

Aerodynamic Noise Simulation of a High-Speed Maglev Train Operating inside a Fully Enclosed Sound Barrier

Y. H. Chen¹, J. M. Ge^{1†} and S. Liu²

¹ School of Physics Science and Engineering, Tongji University, Shanghai, 200092, China

² Appraisal Center for Environment & Engineering, Ministry of Ecology and Environment, Beijing, 100012, China

†Corresponding Author Email: jmge@tongji.edu.cn

(Received July 26, 2022; accepted October 12, 2022)

ABSTRACT

The aerodynamic noise from the new high-speed Maglev train (NHMT) is significant. One way to reduce it is to use a fully enclosed sound barrier (FESB). This paper studies the aerodynamic noise characteristics of the NHMT operating inside a FESB at 600 km/h, taking into account the compressibility of air and the quadrupole sound sources. The transient flow field around the NHMT is simulated by adopting an improved delayed detached-eddy simulation. According to Lighthill acoustic analogy theory, the aerodynamic noise inside and outside the FESB can be simulated using the acoustic finite element method. The sound insertion loss (IL) of the FESB is analyzed by comparing the noise outside the FESB with the noise generated by the NHMT operating on open tracks. The results indicate that the noise is distributed in the streamlined shoulder area of the head and tail car and the wake. The far-field noise belongs to broadband noise, and the noise outside the FESB is similar to an incoherent line source. The IL of the FESB is 25.2 dB(A) at 25 m from the track centerline and 3.5 m above the track surface. Therefore, the noise reduction effect of a FESB is much better than a traditional upright sound barrier.

Keywords: High-speed Maglev train; Aerodynamic noise; Fully enclosed sound barrier; Acoustic finite element method; Insertion loss.

1. INTRODUCTION

With the increasing demand for rapid travel, current high-speed wheel-rail trains can no longer meet the demand. Maglev trains are being studied because of their excellent high speed, smooth running, safety, and energy-saving. These trains use an electromagnetic suspension system which consists of an onboard electromagnet that attracts a stator core on the track (Deng *et al.* 2019). As a result, the train "floats" above the track.

There are mainly three noise sources for Maglev trains: aerodynamic, equipment, and structure-borne noise. Since the radiated power of the dipole and quadrupole aerodynamic noise is proportional to the 6th and 8th power of the train speed, aerodynamic noise becomes predominant as the train operates at speeds greater than 300 km/h (Mellet *et al.* 2006). Excessive aerodynamic noise leads to noise pollution, which limits further speed (Cao *et al.* 2021). Fully enclosed sound barriers (FESBs) can cover all the aerodynamic noise sources in an internal space without noise diffraction. This technique is the most effective way to reduce the noise (Zheng *et al.*

2021). To minimize it, a detailed understanding of the flow and sound field characteristics is essential.

Only a few Maglev trains are operating worldwide. Therefore, studies of their aerodynamic performance and noise are lacking. The current research on aerodynamic noise includes experimental and numerical simulations. Experimental research consists of wind tunnel tests and line tests. Tyll *et al.* (1996) built a wind tunnel with a high-speed moving track to study the aerodynamic performance of a 1/12th scaled TR06 Maglev train model with a wind speed of 241 km/h. They measured the aerodynamic force coefficients and analyzed the flow field characteristics in the transverse and longitudinal sections. Ding *et al.* (2020) performed an experimental study of a 1/8th scaled Maglev train model in a wind tunnel. They obtained the aerodynamic lift coefficients for each carriage and the pressure coefficient distribution in the longitudinal section. Katsuya *et al.* (2004) conducted line tests of a new Maglev train running on the Yamanashi Maglev Test Line. They measured the pressure amplitude of the tunnel wall when the train ran at 500 km/h. Li *et al.* (2006)

conducted actual train tests on the TR08 Maglev train when it operated on the Shanghai Maglev Line. The magnitude of the pressure wave was obtained when the trains met at 400~500 km/h. Duan *et al.* (2010) conducted field tests on the external noise generated by the low and medium-speed Maglev train. The results indicated that the sound energy is concentrated within 500~2000 Hz as the train runs at 20~75 km/h. They also found that the Maglev train has less radiation noise than the wheel-rail train, with other conditions unchanged. The pass-by noise of the TR08 Maglev train was tested in Emsland, and the sound exposure levels (SELs) at different distances from the track were recorded when the train was running on different types of tracks (Barsikow *et al.* 2002). The results showed that the SEL at 25 m from the line reaches 94 dB(A) when the train operates at 400 km/h. Chen *et al.* (2007) tested the external noise generated by the TR08 Maglev train running on the Shanghai Maglev Line. The results showed that the maximum A-weighted sound pressure level (SPL) at 30 m from the track is 94.7 dB(A) when the train operates at 430 km/h. The SPL declines by 6~8 dB(A) as the distance is doubled.

The numerical simulation method has gradually become popular for fluid dynamics research and aerodynamic noise prediction because it costs a shorter period and can predict the aerodynamic noise generated under different inflow conditions. The Aero-Acoustic Analogy (AAA) is the commonly utilized method in the simulation of aerodynamic noise. This method is a two-step process. First, the unsteady flow is simulated by computational fluid dynamics (CFD) to obtain equivalent sound sources. Then the noise at the monitoring points is calculated by FW-H integral equation or acoustic finite element method (FEM) (Thompson *et al.* 2015). Bi *et al.* (2004, 2005) estimated the aerodynamic force and the flow characteristics of the TR Maglev train based on the compressible N-S equations. The results indicated that the airflow velocity around the train decreases with increasing distance from the train surface. Zhou *et al.* (2020) simulated the flow around the new Maglev train operating at 600 km/h by adopting the improved delayed detached-eddy simulation method (IDDES). The results showed that the train has better aerodynamic load performance, and the vortex has irregular and random distribution characteristics in the wake. Huang *et al.* (2019) used the unsteady compressible numerical simulation to study the flow field when the two trains crossed at 430 km/h. The transient pressure change was analyzed, and the safe trackside distance was determined. Jia and Mei (2018) used the 1D compressible unsteady non-homentropic flow model to investigate the pressure wave produced by the Maglev train running inside the tunnel at 400~650 km/h and determined the critical tunnel length. Zhang *et al.* (2021) calculated the aerodynamic noise of the Maglev train operating at 600 km/h by adopting the large eddy simulation (LES) and K-FWH equations. The results showed that the radiation energy of the quadrupole sound sources is higher than that of the

dipole sound sources and occupies the dominant position for the far-field monitoring points. Su *et al.* (2018) combined the detached-eddy simulation (DES) and FW-H equation to simulate the flow field and aerodynamic noise of the high-speed train operating on the bridge. The results showed that the far-field noise is broadband noise, with the primary energy centralized within 630~5000 Hz. Tan *et al.* (2019) adopted the LES method and K-FWH equations to simulate the aerodynamic noise of a 600 km/h train. Their results showed that the noise contribution of the quadrupole at the downstream points is more significant than at the upstream points. In addition, the primary energy of the quadrupole tends to be low frequency. Tan *et al.* (2018) utilized the compressible LES model to calculate the flow around a 300 km/h train operating in the tunnel and obtained the spectral characteristics of the noise.

Installing sound barriers is a common approach to reducing the external noise of rail vehicles. Traditional upright sound barriers have a limited effect due to insufficient height, especially for high-rise buildings (Lee *et al.* 2019). The FESB has an enclosed top, which can block the diffraction of noise and effectively enhance the noise reduction effect. Consequently, the FESB is being gradually applied in rail transit projects (Wen *et al.* 2021). Li *et al.* (2021) conducted an on-site experiment to analyze the vibration response of the FESB of a railway bridge when the train passed through and proposed the numerical model for evaluating the vibration response. Zheng *et al.* (2021) established a statistical energy analysis model of the FESB. They analyzed the influence of train speeds, structures, and materials of the FESB on sound insertion loss (IL). The results showed that the sound IL of the FESB is better than an upright sound barrier, especially for the high-frequency components. Zheng *et al.* (2022) also used the fast multipole boundary element method to simulate the structure-borne noise of the bridge-FESB system under the wheel-rail excitation. The results indicated that the distribution characteristics of the structure-borne noise vary significantly after the bridge is installed with the FESB. The noise energy of the structure-borne noise of the engineered cementitious composite FESB is mainly concentrated within 50~63 Hz.

Many studies have been carried out on the aerodynamic performance of the Maglev train. Still, there are few experimental and simulation studies on aerodynamic noise. In addition, the FESB is a new type of sound barrier with even less research on the aerodynamic noise reduction effect. This study takes the new high-speed Maglev train (NHMT) as the research target. The IDDES model is utilized to calculate the transient flow around a train inside the FESB at 600 km/h. The acoustic FEM is utilized to calculate the sound field inside and outside the FESB, and the noise spectrum and spatial distribution characteristics are analyzed. The IL of the FESB is analyzed by comparing the noise outside the FESB with the noise generated by the NHMT operating on open tracks.

2. NUMERICAL METHODOLOGY

2.1 Improved Delayed Detached-Eddy Simulation (IDDES)

DES is a hybrid model for solving the transient flow field by combining the unsteady Reynolds-Averaged Navier-Stokes (URANS) model and the LES model. The URANS and LES methods are utilized to simulate the small-scale vortex pulsation near the wall and the large-scale vortex motion far from the wall, respectively. This hybrid method ensures high computational accuracy, reduces the number of grids, and improves computational efficiency (Spalart 1997; Menter *et al.* 2003; Li *et al.* 2020). However, in the case of high aspect ratio grids near the wall, the DES model may switch to the LES model in advance, resulting in grid-induced separation, making the calculated Reynolds number and vortex viscosity coefficient lower than the actual values. Spalart *et al.* (2006) and Reddy *et al.* (2014) proposed the delayed detached-eddy simulation (DDES) to solve this problem by bringing in transition and constraint functions. However, the DDES model suffers from the logarithmic layer mismatch. The IDDES model was developed by Shur *et al.* (2008) to address this issue by introducing a new subgrid length scale.

The IDDES model has been broadly employed to calculate the flow field of delivery vehicles (Li *et al.* 2019; Xia *et al.* 2017). The transport equations of the IDDES model based on the shear-stress transport (SST) k - ω model can be expressed as (Gritskevich *et al.* 2012)

$$\frac{\partial(\rho k)}{\partial t} + \frac{\partial(\rho k u_i)}{\partial x_i} = \frac{\partial}{\partial x_j} [(\mu + \sigma_k \mu_t) \frac{\partial k}{\partial x_j}] + P_k - \rho \sqrt{k^3} / l_{IDDES} \quad (1)$$

$$\frac{\partial(\rho \omega)}{\partial t} + \frac{\partial(\rho \omega u_i)}{\partial x_i} = \frac{\partial}{\partial x_j} [(\mu + \sigma_\omega \mu_t) \frac{\partial \omega}{\partial x_j}] + \alpha \frac{\rho}{\mu_t} P_k - \rho \beta \omega^2 + \frac{2\rho \sigma_{\omega,2} (1 - F_1)}{\omega} \frac{\partial k}{\partial x_j} \frac{\partial \omega}{\partial x_j} \quad (2)$$

Here t , ρ , k , ω , and μ are the time, density, turbulence kinetic energy, specific turbulence dissipation rate, and molecular viscosity. x_i is the Cartesian coordinate component, and u_i is the velocity component. σ_k and σ_ω are the turbulent Prandtl numbers for k and ω , respectively,

$$\sigma_k = F_1 \cdot \sigma_{k,1} + (1 - F_1) \cdot \sigma_{k,2} \quad (3)$$

$$\sigma_\omega = F_1 \cdot \sigma_{\omega,1} + (1 - F_1) \cdot \sigma_{\omega,2} \quad (4)$$

where F_1 denotes the blending function,

$$F_1 = \tanh(\phi_1^4) \quad (5)$$

$$\phi_1 = \min \left[\max \left(\frac{\sqrt{k}}{0.09 \omega y}, \frac{500 \mu}{\rho \omega y^2} \right), \frac{4 \rho k \sigma_{\omega,2}}{y^2 \cdot \max \left(\frac{2 \rho \sigma_{\omega,2}}{\omega} \frac{\partial k}{\partial x_j} \frac{\partial \omega}{\partial x_j}, 10^{-10} \right)} \right] \quad (6)$$

Here y is the distance to the nearest wall. μ_t is the turbulent viscosity,

$$\mu_t = \rho a_1 k / \max(a_1 \omega, F_2 \cdot S) \quad (7)$$

where S is the magnitude of the strain rate tensor, and F_2 is also the blending function,

$$F_2 = \tanh \left\{ \left[\max \left(\frac{2\sqrt{k}}{0.09 \omega y}, \frac{500 \mu}{\rho \omega y^2} \right) \right]^2 \right\} \quad (8)$$

P_k denotes the generation of turbulence kinetic energy due to mean velocity gradients,

$$P_k = \min(\mu_t S^2, 0.9 \rho k \omega) \quad (9)$$

The IDDES length scale l_{IDDES} can be expressed as

$$l_{IDDES} = f_d \cdot (1 + f_e) \cdot \sqrt{k} / (0.09 \omega) + (1 - f_d) \cdot C_{DES} \Delta \quad (10)$$

$$\Delta = \min[0.15 \cdot \max(y, h_{\max}), h_{\max}] \quad (11)$$

Here f_d , f_e , and h_{\max} are the empiric blending function, the elevating function, and the maximum edge length of the cell. α , β , $\sigma_{k,1}$, $\sigma_{k,2}$, $\sigma_{\omega,1}$, $\sigma_{\omega,2}$, a_1 , and C_{DES} are the empirical constant.

2.2 Acoustic Finite Element Method (FEM)

The AAA method divides the acoustic simulation into two steps. The unsteady flow equations are solved by using CFD at first. The second step is to extract sound sources from the CFD results and solve the acoustic wave equation. The AAA method decouples the acoustic wave equation and the flow equations, improving the computational efficiency (Sun and Xiao 2018). Lighthill (1951, 1954) obtained the aerodynamic noise wave equation based on the basic equations of fluid dynamics, which can be expressed as

$$\left(\frac{\partial^2}{\partial t^2} - c_0^2 \nabla^2 \right) \rho = \frac{\partial^2 T_{ij}}{\partial x_i \partial x_j} \quad (12)$$

where c_0 is the speed of sound and T_{ij} is the Lighthill stress tensor, which can be expressed as

$$T_{ij} = \rho u_i u_j + (p - c_0^2 \rho) \delta_{ij} - \tau_{ij} \quad (13)$$

Here p is the pressure, τ_{ij} is the viscous stress tensor, and δ_{ij} is the Dirac delta function. The Lighthill equation is transformed from the time domain to the frequency domain by performing the Fourier transform as follows:

$$-\omega_0^2 \rho - c_0^2 \nabla^2 \rho = \frac{\partial^2 T_{ij}}{\partial x_i \partial x_j} \quad (14)$$

Here ω_0 is the circular frequency of the sound wave. The FEM is a commonly used method for numerically solving acoustic problems. Its basic idea is to divide the continuous fluid medium into many small cells with common nodes and express the continuously distributed physical quantities as a combination of physical quantities on discrete nodes. Thus, this method converts the continuous problem into a discrete one (Caro *et al.* 2004). To solve Eq.

(14), the shape function N_a is used as the test function. The left and right sides of Eq. (14) are multiplied by N_a and performed volume integration, and the solution that makes the integral equation hold is the approximate solution of the equation. This method is called the Galerkin method, and the integral equation can be expressed as

$$\iiint_V N_a \cdot (-\omega_0^2 \rho - c_0^2 \frac{\partial^2 \rho}{\partial x_i^2}) dV = \iiint_V N_a \cdot \frac{\partial^2 T_{ij}}{\partial x_i \partial x_j} dV \quad (15)$$

Using partial integration, the Gauss theorem and the momentum conservation equation, Eq. (15) can be written as

$$\begin{aligned} \omega_0^2 \iiint_V N_a \rho dV - \iiint_V \frac{\partial N_a}{\partial x_i} c_0^2 \frac{\partial \rho}{\partial x_i} dV = \\ j\omega \iint_S N_a \rho u_i n_i dS + \iiint_V \frac{\partial N_a}{\partial x_i} \frac{\partial T_{ij}}{\partial x_j} dV \end{aligned} \quad (16)$$

Here n_i is the component of the normal unit vector of the integral surface. The left side of Eq. (16) is the acoustic propagation operator, and the right side of Eq. (16) is the sound source terms, which are extracted from the CFD results. The first term on the right side of Eq. (16) represents the surface source term, and the second represents the volume source term.

3. COMPUTATIONAL MODEL AND VERIFICATION

3.1 Geometric Model

Taking the NHMT as the research object and the train surface, track and FESB are established by using the 3D modeling software. The simplified NHMT model is depicted in Fig. 1. The Maglev train model consists of three cars, namely, the head car (HC), the middle car (MC), and the tail car (TC), and the shape of the HC and TC are the same. The train surface is simplified to a smooth curved surface, and specific uneven components like doors, windows, and windshields on joints are neglected. The length of the HC is 28 m, of which the streamlined length is about 16 m. The length L , width W , and height H of the MC are 25 m, 3 m, and 4.2 m, respectively.

Figure 2 depicts the cross-section of the train, track, and inner wall of the FESB model. The double-track tracks are adopted in this model. The height of the track surface is 1.3 m, and the distance between the two tracks is 5 m. The inner wall of the FESB is modeled as a smooth arched profile, and the complex and detailed parts, such as ribs and purlins, are neglected. The inner wall of the FESB is fan-shaped, with a radius of 6.07 m and an area of 91.2 m². When an NHMT runs inside a FESB, the blockage ratio is 0.108.



Fig. 1. Geometric model of the NHMT.

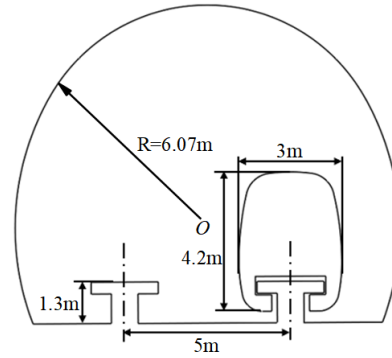


Fig. 2. The cross-section of the train, track, and inner wall of the FESB.

The premise of calculating the external noise of the FESB is to understand the structural components of the FESB in detail and to establish a specific geometric model. Since currently there is no FESB for high-speed Maglev trains, the composite metal sound insulation boards used in the FESB of the Shenzhen-Maoming highspeed railway passenger dedicated line are adopted in this study. The overall thickness of the sound insulation board is 140 mm, composed of a perforated aluminum panel of 1 mm, a sound-absorbing layer made of centrifugal glass wool with a thickness of 137.5 mm, and an aluminum alloy slab with a thickness of 1.5 mm. This structure is shown in Fig. 3. The aperture of the perforated plate is not more than 2.5 mm, and the perforation rate is 30% (Zheng *et al.* 2022). This study focuses on the aerodynamic noise sources inside the FESB and the air-borne noise transmitted to the external space through the FESB. The structure-borne noise generated by the bridge and the FESB is not involved, so the bridge and pier are not considered in the model.

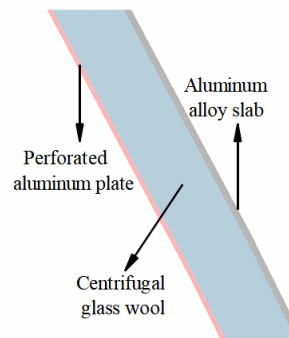


Fig. 3. Local model of the FESB.

3.2 Computational Domain, Boundary Conditions, and Model Parameters

The computational domain size mainly depends on the accuracy and memory requirements. The computational domain of the flow of the NHMT inside the FESB is shown in Fig. 4. It is convenient to take the operation direction of the NHMT (the negative direction of the x-axis) as the reference, and the train runs on the right track. The inlet is $8L$ from the nose tip of the HC, and the outlet is $13L$ from the nose tip of the TC to ensure sufficient flow development in the wake.

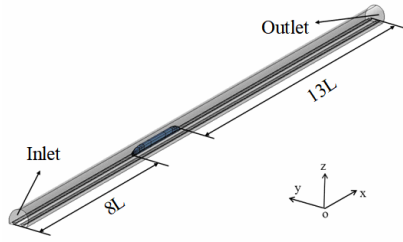


Fig. 4. Computational domain of the flow field.

The fluid's compressibility should be considered as the Mach number exceeds 0.3 (Fraser-Mitchell 2012). The NHMT runs at 600 km/h, corresponding to the Mach number of 0.49, not to mention that the train operates inside the FESB, leading to a significant air compression effect. Hence, flow compressibility needs to be considered.

The inlet is designated to the pressure far-field boundary condition, the pressure and Mach number on which equals one standard atmospheric pressure and 0.49, respectively, and the airflow direction is along the x-axis. The outlet is designated to the pressure outlet boundary condition and the pressure on which is also 1 atm. According to the idea of relative motion, the track and inner wall of the FESB are designated to the slip wall at 600 km/h. The surface of the NHMT is set to the fixed wall with a non-slip condition.

The computational domain of the sound field of the NHMT is depicted in Fig. 5. The dimension of the acoustic solving domain is determined according to the CFD results so that the computational domain can contain the regions with high vorticity and turbulence kinetic energy in the flow field. The distance from the nose tip of the HC to the inlet is L . Because the vortex in the wake extends a longer distance downstream, the distance from the nose tip of the TC to the outlet is $2L$. The thickness of the outer air domain is 1.2 m.

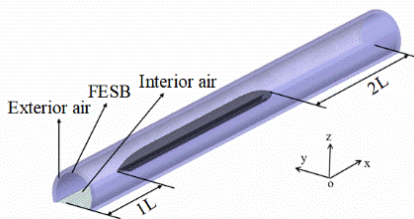


Fig. 5. Computational domain of the sound field.

The inner layer of the FESB is set as a perforated shell component, the middle layer adopts the Delany-Bazley porous model, the outer layer is defined as a solid shell layer, and the material in the interior and exterior air domains is designated to air. The inlet and outlet of the FESB are defined as non-reflecting boundary conditions, the interior air domain is assigned to the Lighthill sound source boundary condition, and the source data is converted from the CFD results. The surface of the NHMT and the track are rigid walls, and the boundary of the exterior air is set as the infinite element surface, which can model the unbounded acoustic domain and compute the far-field noise.

3.3 Meshing Strategy

The numerical precision of the flow field calculation is closely associated with the quality and quantity of the meshes. The meshing results are depicted in Fig. 6. The computational domain of the flow field is discretized by unstructured meshes. The NHMT and the track surface are discretized by triangular meshes, and the maximum mesh size is 80 mm and 100 mm, respectively. Appropriate mesh refinement is performed for curved surfaces with large curvatures. To accurately capture the flow features near the train surface and vortex structures in the wake, ten layers of the boundary layer mesh are performed on the train surface, wherein the thickness of the first layer is 0.05 mm, and the mesh growth rate is 1.2. Additionally, the meshes of the area close to the train surface and in the wake need to be refined, and the maximum mesh size of the encrypted area does not exceed 300 mm. Amount of meshes in the computation domain of the flow is approximately 28 million.

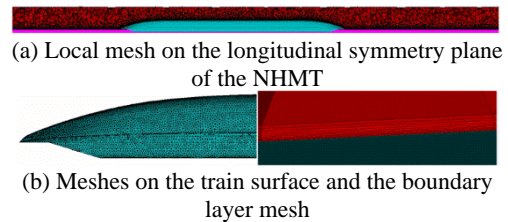


Fig. 6. Local mesh distribution of the computational domain of the flow.

The meshing results of the sound field computational domain are depicted in Fig. 7. The acoustic meshes are generally homogeneous, and the wavelength of the acoustic wave corresponding to the maximum analysis frequency should be at least four times the size of the elements with high order. The highest frequency analyzed in this paper is 3500 Hz, so the largest size of acoustic meshes is 25 mm. The sound field computational domain consists of about 22 million cells in total.



Fig. 7. Local mesh distribution of the computational domain of the sound field.

3.4 Solver Description

The steady flow field is solved by adopting the SST $k-\omega$ model, and the simulation results are treated as the initial conditions for the transient flow simulation. The IDDES model based on the SST $k-\omega$ model is selected for the transient flow field calculation. For both steady and unsteady flow field simulations, the semi-implicit method for the pressure-linked equation (SIMPLE) algorithm is utilized for the pressure-velocity coupling. The discretization schemes of equations adopted for CFD are listed in Table 1. The transient time step Δt is 0.0001 s, so the maximum analysis frequency is 5000

Hz. The total number of calculation time steps is 2000. The first 1000 steps are calculated for the sufficient evolution of the turbulence. The transient flow data of each time step is recorded for the remaining 1000 steps to extract the aerodynamic noise sources. Therefore, the total time is 0.1 s, and the frequency resolution is 10 Hz.

Table 1 Discretization schemes of equations

Equation	Steady	Transient
Momentum	Second-order upwind	Bounded central differencing
Continuity	Standard	
Energy	Second-order upwind	
Turbulence kinetic energy	Second-order upwind	
Specific turbulence dissipation rate	Second-order upwind	
Transient formulation	/	Bounded second-order implicit

Based on Lighthill acoustic analogy theory, the transient flow data obtained from the CFD results for each time step is converted to Lighthill sound sources. Then the sources are converted from the time domain to the frequency domain by performing the discrete Fourier transform (DFT). Since the computational domain and meshes of the flow and sound field calculation model are different, it is necessary to map the sound sources from the flow field meshes to the acoustic meshes. The acoustic FEM is subsequently utilized to simulate the near- and far-field noise (Hou *et al.* 2021).

The CFD simulation and aeroacoustic computation were performed by the Ansys Fluent and Actran software, respectively. The numerical simulations were carried out on a high-performance parallel computation platform with 112 CPUs. It took about 125 and 105 h to complete the flow field and acoustic computation, respectively.

3.5 Validation

For the purpose of validating the numerical simulation method for calculating the aerodynamic noise generated by the NHMT, which has not yet rolled off the assembly line, the TR08 Maglev train operating on the Shanghai Maglev line is used in this section, as shown in Fig. 8(a) (Deng *et al.* 2022). There is little difference between the NHMT and the TR08 train in major dimensions such as width and height, while the main difference is that the TR08 train has a shorter streamlined length of 5.2 m. Since the Shanghai Maglev line does not have the FESB or tunnel section, a real train test of the TR08 Maglev train operating on the open tracks at 430 km/h was conducted. Two types of sensors were arranged in the trial. A surface microphone was mounted at the outer window of the TC to test the SPL on the train surface during the train operation. Two free-field microphones used to test the pass-by noise were arranged at 7.5 m and 30 m from the track centerline, respectively. The two microphones were both 1.2 m

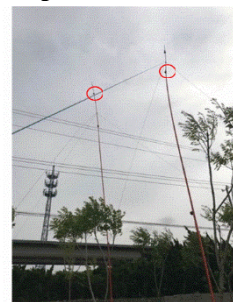
above the track surface and in the same cross-section perpendicular to the track. The test was conducted in windless weather, at least eight sets of valid data were measured, and the equivalent continuous A-weighted sound pressure level (ECASPL) spectrum results were averaged over all sets during the pass-by time. Figure 8(b) and (c) show the arrangement of the microphones at the test site.



(a) The TR08 Maglev train



(b) Surface microphone



(c) Far-field microphones

Fig. 8. Real train test site.

The computational domain of the flow of the TR08 Maglev train operating on the open tracks is depicted in Fig. 9. The simplified TR08 train model consists of three cars, and the length L_0 , width W_0 , and height H_0 of the MC are 25 m, 3.7 m, and 4.2 m, respectively. The nose tip of the HC is L_0 from the inlet, and the nose tip of the TC is $3L_0$ from the outlet. The distance from the track surface to the bottom surface of the computational domain is $2H_0$, and the width and height of the computational domain are $6W_0$ and $5H_0$, respectively. The cross-section ABCD is set as the pressure far-field boundary condition, and the pressure and Mach number are 1 atm and 0.35. The cross-section EFGH is designated to the pressure outlet boundary condition and the pressure on which is 1 atm. The cross-section CDHG and the track surface are assigned to the slip wall with a speed of 430 km/h. The cross-section ADHE, BCGF, and ABFE are assigned to symmetric boundary conditions, and the train surface is designated as the fixed wall.

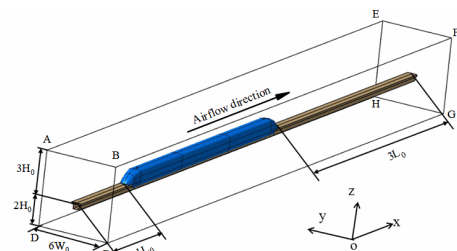


Fig. 9. Computational domain of the flow of the TR08 Maglev train.

The surface point is situated at the outer window of the TC, which corresponds to the position of the surface microphone in the actual train test. Two rows of the noise monitoring points, 1.2 m above the track surface, are evenly arranged along the x-axis at 7.5 m and 30 m from the track, respectively. The distance between each two adjacent longitudinal points is 2 m, and the points at the two ends of each row are in the same cross-section with the nose tip of the HC and the TC, respectively.

For calculating the flow and sound field of the TR08 Maglev train operating on the open tracks, the meshing strategy, turbulence model, and numerical calculation method are used, as elaborated in Sections 3.3 and 3.4. Figure 10 compares the 1/3 octave spectral curves of the SPL at the surface monitoring point of the TR08 Maglev train between the real train test and simulation. It can be observed that the noise energy of the train surface is mainly centralized within 630~2500 Hz, and the two SPL spectral curves have the same variation trend. The difference between the test and simulation does not exceed 2 dB(A) in each frequency band except at 3150 Hz.

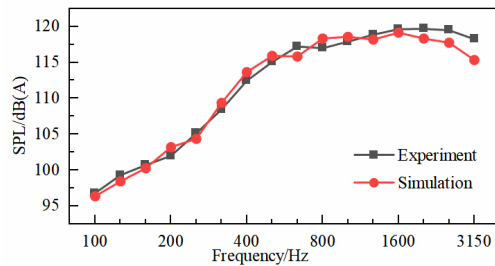


Fig. 10. Comparison of the 1/3 octave spectral curves of the SPL at the surface monitoring point between the real train test and simulation.

By averaging the A-weighted SPL spectral data calculated from all the far-field points in the same row, the ECASPL spectrum results during the pass-by time can be obtained approximately. Figure 11 compares the 1/3 octave spectral curves of the ECASPL at the far-field points between the real train test and simulation. The far-field noise energy is mostly centralized within 800~2000 Hz, and good agreement between the two ECASPL spectral curves is observed in terms of spectral shape. The difference between the test and simulation does not exceed 2 dB(A) when the frequency is below 2000 Hz. The difference is relatively significant at frequencies above 2500 Hz but no more than 4 dB(A). The meshes cannot accurately capture the delicate vortex structures, resulting in low simulation results at high frequency. The far-field aerodynamic noise energy is mainly concentrated below 2 kHz, so the difference has a minor impact on calculating the overall sound pressure level (OASPL) at the far-field monitoring points.

Table 2 compares the OASPL between the test and simulation. The difference of the OASPL on the train surface is 0.6 dB(A), and the difference at the far-field monitoring points does not exceed 1.5 dB(A). The high agreement between the test and simulation

of the aerodynamic noise generated by the TR08 Maglev train running on the open tracks indicates that the simulation model is accurate. It also indirectly shows that the turbulence model, meshing strategy, and numerical calculation method used in this paper are reliable and valid for simulating the flow and sound field of the NHMT. The following sections, 4 and 5, show the simulation results of the NHMT operating inside the FESB at 600 km/h.

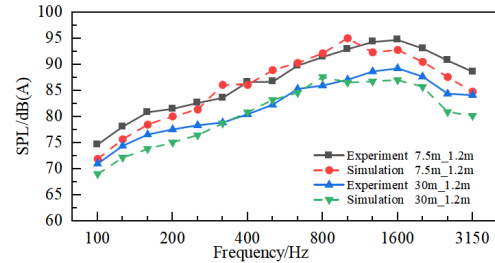


Fig. 11. Comparison of the 1/3 octave spectral curves of the ECASPL at the far-field points between the real train test and simulation.

Table 2 Comparison of the OASPL between the test and simulation

Location	Train surface	7.5 m_1.2 m	30 m_1.2 m
Test/dB(A)	128.1	101.9	96.6
Simulation/dB(A)	127.5	101.3	95.4
Difference/dB(A)	0.6	0.6	1.2

4. FLOW FIELD CHARACTERISTICS

Accurate transient flow calculation around the NHMT inside the FESB at 600 km/h is the basis for obtaining the aerodynamic noise sources. Figure 12 depicts the velocity distribution around the NHMT. It could be found that the airflow first contacts the nose tip of the HC and is blocked by it. The flow velocity decreases sharply, a stagnation zone is formed in this region, and the local pressure reaches the maximum. Restricted by the inner wall of the FESB, the air is constantly compressed when it flows through the streamlined area of the HC, and the flow velocity is also increasing. When the airflow flows over the streamlined area of the HC, the blockage ratio reaches the maximum and remains constant. The flow velocity reaches a maximum and remains unchanged from the HC to the TC. The flow velocity is about 1.17 times the free incoming flow velocity. When the airflow flows through the streamlined area of the TC, the blockage ratio decreases, the air expands, and the flow velocity decreases gradually. The flow velocity in the wake is small and extends downstream for a long distance due to vortex shedding.

With the high-speed movement of the NHMT, plenty of vortices are inevitably generated, especially in the wake. Figure 13 depicts the vorticity spatial distribution in the x-y plane 0.5 m above the track surface. The strong vorticity is located near the train

surface and in the wake. The distribution of high vorticity regions in the wake has the shape of strips because of the flow separation around the TC. A large vortex pair is formed from the streamlined shoulder of the TC with an opposite rotation direction, which extends in the downstream direction.

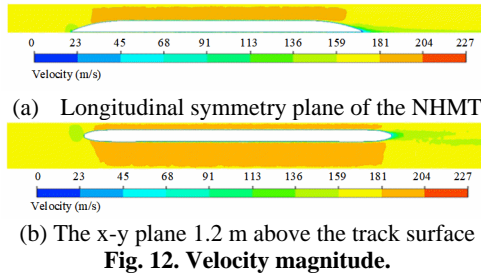


Fig. 12. Velocity magnitude.

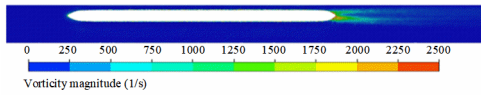


Fig. 13. Vorticity magnitude on the x-y plane 0.5 m above the track surface.

According to the theory of vortex sound, aerodynamic noise is generated by the movement of vortices in the unsteady fluid flow (Powell 1964). The Q criterion is a standard method for identifying vortex structures (Hunt *et al.* 1988). It can be expressed as follows:

$$Q = (\Omega_{ij}\Omega_{ij} - S_{ij}S_{ij})/2 \quad (17)$$

Here Ω_{ij} and S_{ij} are the anti-symmetric and symmetric terms of the velocity gradient tensor, respectively.

Figure 14 depicts the spatial distribution of the 3D vortex structures in the wake based on the Q criterion, colored by the velocity magnitude. The Q-value of Fig. 14(a) and (b) are 4000 s^{-2} and 10000 s^{-2} , respectively. Some small-scale vortices are attached to the train surface in the rear area of the TC, and aerodynamic noise is generated by the turbulent boundary layer (TBL) with relatively low energy. In the streamlined shoulder region of the TC, the flow separation occurs at the train surface. The wake region is filled with vortices of different scales and intensities, the most prominent of which are the counter-rotating vortex pair with considerable energy, and the vortex pair expands slightly in the spanwise and vertical direction as it develops. In the process of the vortex moving downstream, the large vortex pair is continuously broken down and reorganized, the energy of which keeps weakening due to the air viscosity effect, and the vortex structures disappear in the end. The larger the Q-value of the iso-surface, the smaller the vortex scale and the larger the vorticity. It could be observed that during the evolution of the vortex structures, the small-scale vortices transfer the vorticity to the large-scale vortices. Therefore, the small-scale vortices are easier to dissipate, and the large-scale vortices

extend downstream for a longer distance than the small-scale vortices.

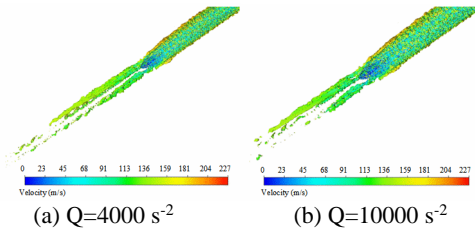


Fig. 14. Instantaneous iso-surface normalized by Q-criterion in the wake (colored by velocity).

4. AERODYNAMIC NOISE CHARACTERISTICS

Based on Lighthill acoustic analogy theory, the transient flow data around the NHMT inside the FESB can be converted into sound sources. The sound sources converted to the frequency domain by implementing the DFT are mapped to the acoustic meshes. Then the acoustic FEM is adopted to calculate the noise inside and outside the FESB. With the same meshing strategy, turbulence model, and numerical simulation method, the far-field aerodynamic noise of the NHMT operating at 600 km/h on the open tracks can be simulated. The FESB's noise reduction effect can be analyzed.

4.1. Internal Aerodynamic Noise Characteristics of the FESB

Figure 15 depicts the arrangement of the points inside the FESB. Five points are placed on the train surface, among which D1 and D2 are in the streamlined region close to the nose tip of the HC and TC, respectively. It is very convenient to use the train running direction (the negative direction of the x-axis) as the reference, and D3, D4, and D5 are located near the top, right, and left areas of the middle of the MC, respectively. Two rows of the points are uniformly placed along the x-axis at locations that are 1.8 m above the track surface and 10 cm from the inner wall of the FESB, numbered E1~E40 and F1~F40, and the distance between each two adjacent longitudinal points is 4 m.

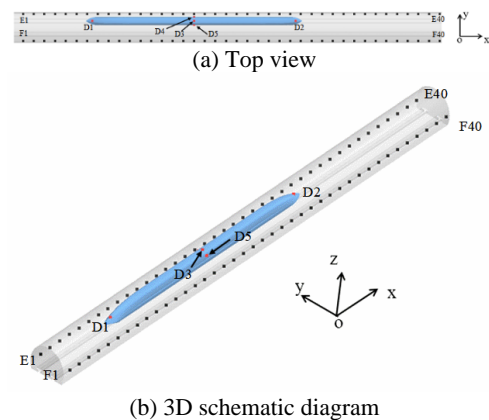


Fig. 15. Layout of the monitoring points inside the FESB.

Figure 16 depicts the spectral curves of the SPL at the points on the longitudinal symmetry plane of the train. The A-weighted SPL at D3 is the lowest among the three points within 100~1600 Hz. When the frequency exceeds 1600 Hz, the three spectral curves have the same trend with a slight difference in each frequency band. It is because the surface of the top of the MC is smooth and flat, where the TBL primarily generates the aerodynamic noise. Thus, the A-weighted SPL is the lowest. The A-weighted SPL at D3 first tends to increase with frequency, reaching the maximum value of 123.1 dB(A) at 1600 Hz. The OASPL of D3 is 128.7 dB(A). When the frequency is below 1000 Hz, the A-weighted SPL at D2 is more prominent than D1, while the A-weighted SPL at D2 is less than D1 when the frequency exceeds 1000 Hz, but the difference is not significant. It could be found from Fig. 14 that a large vortex pair is generated in the wake, whose energy is centralized in the low and middle-frequency bands, so the SPL at D2 is relatively large in these frequency bands. Due to the energy dissipation when the airflow moves along the train surface, the SPL at D2 is slightly lower than D1 in the high-frequency band. The OASPL of D1 and D2 are 133.2 and 136.2 dB(A), respectively.

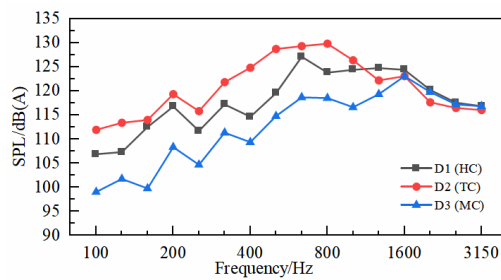


Fig. 16. 1/3 octave spectral curves of the SPL at the points on the longitudinal symmetry plane of the train.

Figure 17 depicts the spectral curves of the SPL at the points in the middle of MC, and the three points are in the same cross-section perpendicular to the track. As can be seen from the figure, the A-weighted SPL at D3 is the lowest in the range of 100~630 Hz. When the frequency is higher than 630 Hz, the difference in A-weighted SPL at the three points is slight in each frequency band except for 1600 Hz. The spectral curves of D4 and D5 have the same trend with frequency, and the A-weighted SPL tends to increase with the frequency at the beginning, reaching peaks of 124.6 and 124.4 dB(A) at 630 Hz, respectively, while the A-weighted SPL does not change with frequency when the frequency exceeds 800 Hz. The OASPL of D4 and D5 are 129.6 and 129.4 dB(A), respectively, which is about 1 dB(A) higher than D3.

Figure 18 depicts the longitudinal distribution curves of the OASPL on the inner walls of the FESB, and $x=0$ m corresponds to the middle of the MC. The OASPL on the left and right inner walls of the FESB has the same trend along the x -axis. The OASPL increases first, reaching the maximum value in the streamlined area of the HC ($x=-32$ m), after which the OASPL gradually decreases. Starting from the

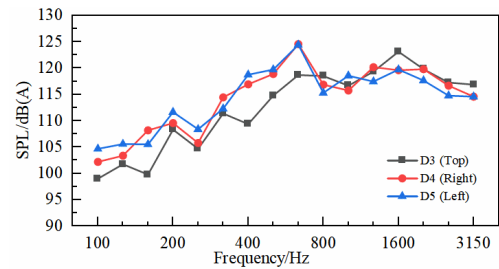


Fig. 17. 1/3 octave spectral curves of the SPL at the points in the middle of MC.

region where the MC is close to the HC ($x=-8$ m), the OASPL increases along the x -axis. Especially in the streamlined part of the TR, the OASPL increases significantly. The OASPL reaches another maximum value in the nose tip area of the TC ($x=40$ m), and then the OASPL gradually decreases. In the longitudinal range, the OASPL on the right inner wall is 0.3~4.8 dB(A) higher than that on the left inner wall of the FESB, especially near the nose of the HC, the MC, the TC, and in the wake. Since the train runs on the right track, the right space inside the FESB is smaller than the left space, the reverberation effect is more pronounced, and the SPL is higher in the right space. The OASPL of the right and left inner walls of the FESB are 123.8 and 120.6 dB(A) at $x=-32$ m, 127.3 and 125.1 dB(A) at $x=40$ m, respectively.

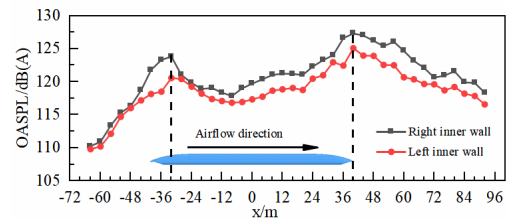


Fig. 18. The OASPL distribution curves along the x -axis.

Figure 19 depicts the spectral curves of the SPL at E27 and F27 ($x=40$ m), whose OASPL reaches the maximum on the inner walls of the FESB along the x -axis, as presented in Fig. 18. It could be observed that the two spectral curves have the same trend with frequency. The A-weighted SPL tends to increase with the frequency at the beginning, reaching peaks of 119.8 and 122.6 dB(A) at 630 Hz, respectively, while the A-weighted SPL decreases rapidly as the frequency is higher than 1600 Hz. The A-weighted SPL of E27 is 0.1~6.7 dB(A) higher than that of F27 in each 1/3 octave band, and the OASPL of E27 is 2.2 dB(A) higher than that of F27.

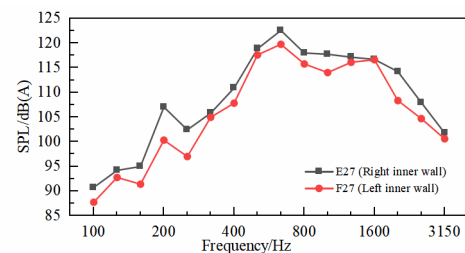


Fig. 19. 1/3 octave frequency spectrum of the SPL on the inner wall of the FESB.

Figures 20 and 21 show the sound field distribution inside the FESB at 630 and 1600 Hz, respectively. The two selected sections are the longitudinal symmetry plane of the train and the x-y plane 1.8 m above the track surface. The SPL is relatively high near the streamlined area of the HC and TC and in the wake at 630 Hz. Since large-scale vortices in the wake extend downstream for a long distance, the region with high sound intensity is widely distributed. The SPL around the train decreases as the frequency increases, and the range of high sound intensity area also decreases. The sound field is more evenly distributed around the train in the high frequency because the small-scale vortices are easier to dissipate in the wake.

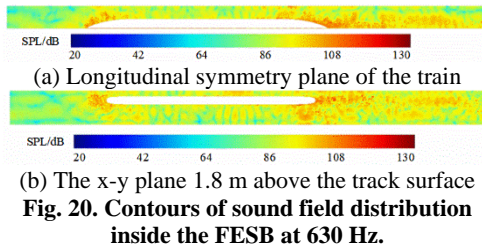


Fig. 20. Contours of sound field distribution inside the FESB at 630 Hz.

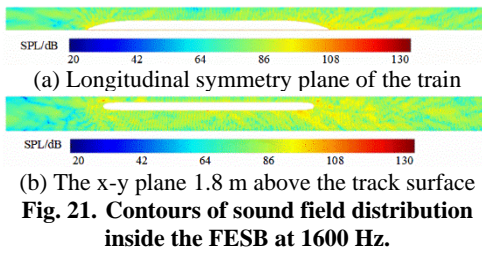


Fig. 21. Contours of sound field distribution inside the FESB at 1600 Hz.

4.2. External Noise Characteristics of the FESB

A series of noise monitoring points are arranged outside the FESB on the right side of the NHMT running direction, as presented in Fig. 22. G1~G32 are placed along the x-axis at 10 cm from the outer wall of the FESB. These points have the same cross-section as E2~E33. The height of these two rows is the same. According to the international standards ISO3095-2013, two rows of the monitoring points are equally spaced along the x-axis at 7.5 m and 25 m from the track centerline, respectively, numbered as H1~H32 and J1~J32, with the distance between each two adjacent longitudinal points being 4 m. These two rows of points are 1.2 m and 3.5 m above the track surface, respectively. Generally, the position 25 m from the track centerline and 3.5 m above the track surface is called the standard far-field position. In the x-y plane 1.2 m above the track surface, three rows of points numbered K1~K7, L1~L7 and M1~M7 are arranged along the y-axis in x=-36 m, 0 m, and 40 m cross-sections, respectively. The lateral distance between the monitoring points and the track are 7.5 m, 10 m, 12.5 m, 15 m, 20 m, 25 m, and 30 m, respectively.

Sound transmission loss (TL) is often employed to assess the sound insulation performance of structures, and it can be expressed as the difference between the incident and transmitted sound power

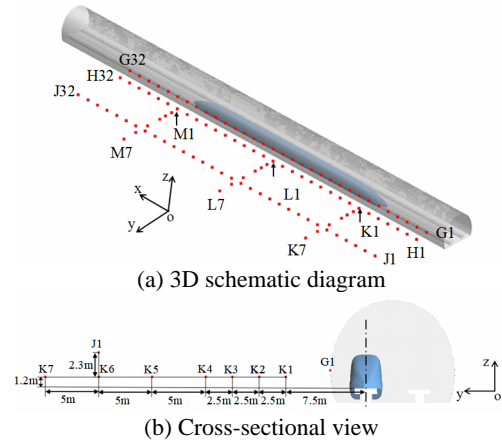


Fig. 22. The layout of the monitoring points outside the FESB.

level. According to the international standards ISO 140-3:1995, TL can be measured in the laboratory, composed of two adjacent reverberation rooms, with an opening between the two rooms accommodating the test specimen. For evaluating the sound insulation effect of the acoustic structure under actual service conditions, noise reduction (NR) is usually adopted in the field. It can be expressed as

$$NR = \bar{L}_{p,inside} - \bar{L}_{p,outside} \quad (18)$$

Here $\bar{L}_{p,inside}$ and $\bar{L}_{p,outside}$ denote the average near-field SPL on the interior and exterior surfaces of the acoustic structure, respectively. The NR is also called the on-site TL. Figure 23 compares the TL of the composite metal sound insulation board used in the FESB between the experiment and simulation. Zhang *et al.* (2019) made measurements in the laboratory. The simulation is the difference between the average SPL of E2~E33 and G1~G32. It can be observed that the curves of the experiment and simulation result are consistent in terms of the trend with frequency. The TL indicates an increasing trend with frequency. In engineering, the average TL is often applied to assess the sound-proof performance of structures, which is defined as the arithmetic mean of the TL of 1/3 octave frequency bands from 100 to 3150 Hz. The maximum difference of the TL between the simulation and experiment results in each frequency band is less than 4 dB, and the average TL is 29.7 and 30.6 dB, respectively, with a lower than 1 dB difference. It demonstrates that this paper's model and simulation method are reliable and can be used for subsequent far-field noise research.

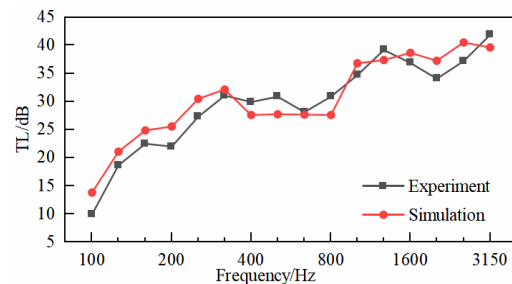


Fig. 23. Comparison of the TL of the FESB between the experiment and simulation.

Figure 24 shows the longitudinal distribution curves of the OASPL outside the FESB, and $x=0$ m still corresponds to the middle of the MC. The distribution curve of the OASPL outside the FESB and on the inner wall has a similar trend in the x -axis direction. The OASPL outside the FESB reaches the local maximum in the streamlined area of the HC ($x=-36$ m) and the nose tip area of the TC ($x=40$ m), and the peak near the TC is 3~5 dB(A) larger than that near the HC. The OASPL of the middle car does not change much along the x -axis direction. The maximum OASPL is 98.0, 84.5, and 79.4 dB(A) at 10 cm from the outer wall of the FESB, 7.5 m, and 25 m from the track centerline, respectively.

The pass-by noise of the NHMT has an impulsive character. The SEL is commonly used to evaluate the noise level, reflecting the total radiated sound energy within the duration of the single noise event. When the SPL decreases by 10 dB, the sound energy decays by 90%. Therefore, for NHMT pass-by noise, when the maximum OASPL is reduced by 10 dB on the time history curve of the OASPL, the time can be taken as the integration time of the SEL. In this paper, when the maximum OASPL is reduced by 10 dB on the OASPL distribution curve along the x -axis, the length interval can be approximated as the integration length of the SEL. It can be expressed as

$$SEL = 10 \lg \left(\int_{x_1}^{x_2} 10^{0.1L_A(x)} dx \right) \quad (19)$$

Here L_A denotes the OASPL, unit: dB(A), x_2 and x_1 represent the upper and lower limits of the integration interval, respectively, and the length of the integral interval can be called the equivalent train length (ETL). As shown in Fig. 24, for the standard far-field position, $x_1 = -46$ m, $x_2 = 64$ m, so the high sound intensity area in the wake covers a broader range than that near the HC. The ETL at this position is 110 m, 29 m greater than the length of the whole train, so the ETL can be approximated by adding the length of the HC to the entire train. The SEL at this position is 94.9 dB(A).

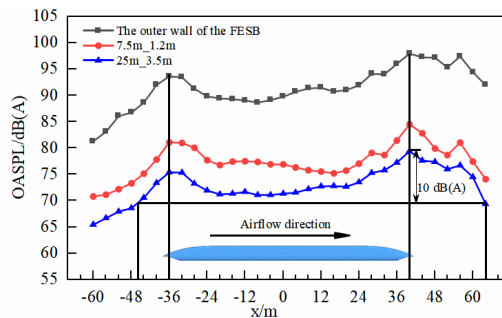
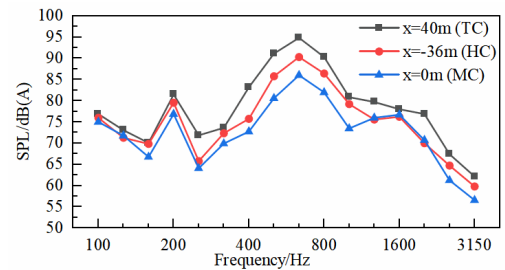


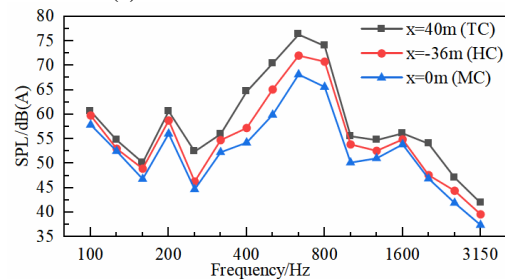
Fig. 24. The OASPL distribution curves along the x -axis outside the FESB.

Figure 25(a) and (b) show the 1/3 octave spectral curves of the SPL on the outer wall of the FESB and 25 m from the track centerline, respectively. The monitoring points are located at the front ($x=-36$ m), the middle ($x=0$ m), and the rear ($x=40$ m) areas of the train. The noise on the outer wall of the FESB belongs to broadband noise. The trend of the SPL with frequency is the same at the three positions,

while the sound energy is concentrated within 400~1000 Hz. The SPL in the rear area of the train is higher than that in the front and central regions of the whole frequency band, especially within 250~1250 Hz. The A-weighted SPL reaches the local maximum at 200 and 630 Hz. The SPL of the train's rear, front, and central areas are 94.9, 90.3, and 86.1 dB (A) at 630 Hz, and the OASPL are 98.0, 93.6, and 89.7 dB (A), respectively. For the standard far-field position, the SPL of different longitudinal distances has the same variation trend with frequency, and the sound energy is centralized within 500~800 Hz. The local maximum of the A-weighted SPL is located at 200 and 630 Hz. The A-weighted SPL at 200 Hz is lower by at least 10 dB (A) than at 630 Hz. The SPL of the train's rear, front, and central areas is 76.4, 72.0, and 68.2 dB (A) at 630 Hz, and the OASPL are 79.4, 75.4, and 71.3 dB (A), respectively. Therefore, to reduce the far-field noise effectively, the TL of the FESB should be improved within the frequency range of 500~800 Hz.



(a) The outer wall of the FESB



(b) The standard far-field position

Fig. 25. 1/3 octave spectral curves of the SPL at the points outside the FESB.

The next step is to investigate the lateral attenuation properties of the external noise of the FESB. The points are placed at the height of 1.2 m from the track surface along the y -axis direction, at the maximum longitudinal OASPL ($x=-36$ m and $x=40$ m), and at the middle of the train ($x=0$ m) cross-sections. Figure 26 shows the transverse attenuation curves of the OASPL in different cross-sections. Since the maximum transverse distance between the outer wall of the FESB and the track centerline is about 3.5 m, the abscissa is set as $\lg(d-3.5)$, where d is the transverse distance between the monitoring point and the track centerline. The transverse attenuation curves of the OASPL in different cross-sections can be fitted linearly, as follows:

$$OASPL_{x=40m} = -7.01 \lg(d-3.5) + 89.1 \quad (20)$$

$$OASPL_{x=-36m} = -7.91 \lg(d-3.5) + 86.1 \quad (21)$$

$$OASPL_{x=0m} = -8.11\lg(d - 3.5) + 82.1 \quad (22)$$

The unit of the OASPL is dB(A). The coefficient of determination R^2 of all fittings is greater than 0.97, indicating an excellent linear relationship between the OASPL outside the FESB and the logarithm of the lateral distance between the sound source and the monitoring point. When the distance from the monitoring point to the outer wall of the FESB is doubled, the noise attenuation is 2.1~2.4 dB(A), which shows that the far-field noise radiation characteristics outside the FESB are like that of the incoherent line source, rather than the point source.

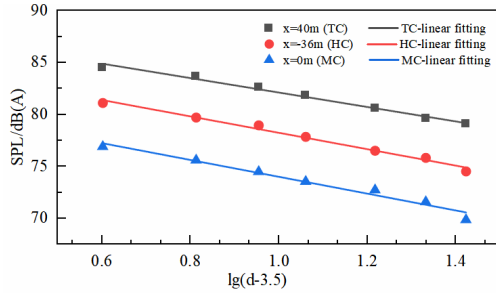


Fig. 26. The OASPL distribution curves along the transverse direction.

Figure 27 shows the sound field distribution outside the FESB in the cross-section at $x=40$ m which has the maximum OASPL along the longitudinal direction. The SPL gradually decreases as the transverse distance increases at 200 Hz, and the SPL is more evenly distributed in the vertical direction when the transverse distance is certain. For noise at 630 Hz, the sound energy is mainly concentrated in 0~6 m in the vertical direction when the lateral distance is 5~17.5 m, and the noise radiation is directional, especially propagating in the obliquely upward direction. The sound energy is more evenly distributed in the vertical direction when the lateral distance is more than 22.5 m. It can be found that the spatial distribution properties of the external noise of the FESB are closely related to the frequency.

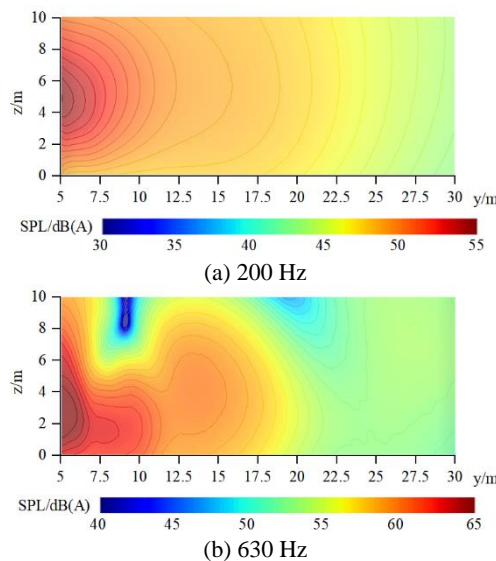


Fig. 27. Contours of SPL distribution outside the FESB at $x=40$ m.

4.3. Noise Reduction Effect

The sound IL can directly reflect the noise reduction effect of the FESB, which is defined as the difference in SPL at a specific location before and after the installation of the FESB, with other conditions guaranteed to be unchanged. In the case of the computation of the flow and sound field of the NHMT running on the open tracks at 600 km/h, the same computational domain, meshing strategy, turbulence model, numerical calculation method, and the layout of the monitoring points are adopted as described in Section 3.5. By averaging the A-weighted SPL spectral data calculated from all the points at the standard far-field position, the ECASPL spectrum result of the NHMT running on the open tracks during the pass-by time can be obtained approximately, denoted as $\bar{L}_{p,before}$. Similarly, by averaging the A-weighted SPL spectral data calculated from the monitoring points J6 to J26 shown in Fig. 22, the ECASPL spectrum result of the NHMT running inside the FESB during the pass-by time can be obtained approximately, denoted as $\bar{L}_{p,after}$. The sound IL can be expressed as

$$IL = \bar{L}_{p,before} - \bar{L}_{p,after} \quad (23)$$

Figure 28 depicts the spectral histogram of the IL at the standard far-field position. It can be found that the spectral result of the IL has the same change trend with frequency as that of the TL shown in Fig. 23. The FESB has a better noise suppression effect in the high-frequency band. The IL of each frequency band is more than 20 dB when the frequency is higher than 200 Hz. According to the simulation results, the ECASPL at the standard far-field position during the pass-by time is 99.2 dB(A) and is reduced to 74.0 dB(A) after the installation of the FESB. It reduces the noise by 25.2 dB(A). The IL of the traditional upright sound barriers is about 10 dB, so the noise reduction effect of the FESB without considering the sound leakage is superior to that of the upright sound barrier (Lee *et al.* 2019).

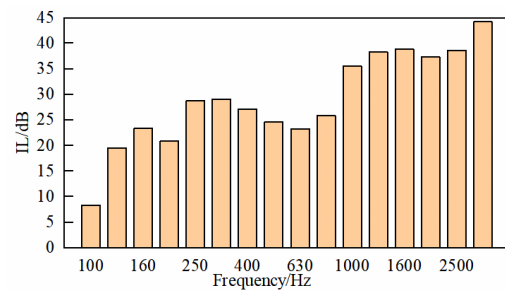


Fig. 28. The IL at the standard far-field position.

5. CONCLUSION

Herein, the IDDES model is utilized to calculate the transient flow around the NHMT inside the FESB at 600 km/h. According to Lighthill acoustic analogy theory, the acoustic FEM is adopted to simulate the aerodynamic noise inside and outside the FESB. Compared with the noise generated by the NHMT running on the open tracks, the noise reduction effect of the FESB is analyzed. The following conclusions

could be derived:

(1) Vortices are the primary source of aerodynamic noise. The flow separation occurs in the streamlined shoulder of the TC, and the wake region is filled with vortices of different scales and intensities, the most prominent of which is the counter-rotating striped vortex pair with considerable energy and extend for a long distance downstream.

(2) For noise on the surface, the SPL in the streamlined area of the TC is larger than the HC when the frequency is less than 1000 Hz. The OASPL on the inner wall of the FESB reaches the local maximum near the streamlined area of the HC and the nose tip of the TC, and the noise energy is mainly concentrated within 500~2000 Hz. The spectral curves of the simulated NR of the FESB and the sound TL measured in the laboratory are consistent with the frequency trend.

(3) The OASPL on the inner wall of the FESB and in the far-field has the same trend along the direction of the train operation. The sound energy is mainly concentrated within 500~800 Hz at the standard far-field position, and the equivalent train length at this position can be approximated by adding the length of the HC to that of the whole train. An excellent linear relationship exists between the OASPL outside the sound barrier and the logarithm of the lateral distance from the sound source to the monitoring point. The far-field noise radiation characteristics outside the sound barrier are similar to the incoherent line source.

(4) The ECASPL during the pass-by time at the standard far-field position is 74.0 dB(A). The IL in each frequency band exceeds 20 dB at this position when the frequency exceeds 200 Hz. The noise is reduced by 25.2 dB(A) after installing the FESB without considering the sound leakage.

The NHMT is being developed rapidly, and the FESBs are gradually promoted for their excellent noise reduction. This work provides a reference for using the FESB to mitigate the exterior noise of the Maglev. It has implications for the optimal design of Maglev trains and FESBs. There are areas needed for further research. For example, the contribution of the structure-borne noise generated by the bridge and the FESB to the far-field monitoring points needs to be considered. The material and structure of the sound insulation boards of the FESB need to be optimized.

ACKNOWLEDGEMENTS

The authors would like to thank the “13th Five-Year Plan” National Key R&D Plan of China (2016YFB1200602) and Major Strategic Projects of Chinese Academy of Engineering (2018-ZD-16) for their support.

REFERENCES

Barsikow, B., D. R. Disk, C. E. Hanson, M. Hellmig, A. Joshi, A. Kupferman, R. Mauri, C. J. Roof and P. Valihura (2002). Noise Characteristics of the Transrapid TR08 Maglev System. Washington: US Federal Railroad

Administration.

Bi, H., B. Lei and W. Zhang (2004). Research on Numerical Calculation for Aerodynamic Characteristics of the TR Maglev Train. *Journal of the China Railway Society* 26(4), 51-54. (In Chinese)

Bi, H., B. Lei and W. Zhang (2005). Numerical Calculation for Turbulent Flow around TR Maglev Train. *Journal of Southwest Jiaotong University* 40(1), 5-8. (In Chinese)

Cao, Y. M., Z. Li, W. Ji and M. Ma (2021). Characteristics analysis of near-field and far-field aerodynamic noise around high-speed railway bridge. *Environmental Science And Pollution Research* 28(23), 29467-29483.

Caro, S., P. Ploumhans and X. Gallez (2004). Implementation of Lighthill's Acoustic Analogy in a Finite/Infinite Elements Framework. *Aiaa/ceas Aeroacoustics Conference*.

Chen, X. H., F. Tang, Z. Y. Huang and G. T. Wang (2007). High-speed maglev noise impacts on residents: A case study in Shanghai. *Transportation Research Part D-Transport And Environment* 12(6), 437-448.

Deng, Z. G., Z. X. Liu, H. T. Li and W. H. Zhang (2022). Development Status and Prospect of Maglev Train. *Journal of Southwest Jiaotong University* 57(3), 455-474. (In Chinese)

Deng, Z. G., Y. Zhang, B. Wang and W. Zhang (2019). Present Situation and Prospect of Evacuated Tube Transportation System. *Journal of Southwest Jiaotong University* 54(5), 1063-1072. (In Chinese)

Ding, S., S. Yao and D. Chen (2020). Aerodynamic Lift Force of High-speed Maglev Train. *Journal of Mechanical Engineering* 56(8), 228-234. (In Chinese)

Duan, C., H. Zhang, Y. Zhu and Q. Qin (2010). Noises of middle-low-speed maglev vehicles. *Applied Acoustics* 29(3), 184-188. (In Chinese)

Fraser-Mitchell, A. H. (2012). Fundamentals of Aerodynamics - Fifth edition. *Aeronautical Journal*.

Gritskevich, M. S., A. V. Garbaruk, J. Schütze and F. R. Menter (2012). Development of DDES and IDDES Formulations for the k- ω Shear Stress Transport Model. *Flow, Turbulence and Combustion* 88(3), 431-449.

Hou, B. W., J. J. Li, L. Gao and D. Wang (2021). Multi-Source Coupling Based Analysis of the Acoustic Radiation Characteristics of the Wheel-Rail Region of High-Speed Railways. *Entropy (Basel)* 23(10), 1-18.

Huang, S., Z. W. Li and M. Z. Yang (2019). Aerodynamics of high-speed maglev trains passing each other in open air. *Journal of Wind Engineering and Industrial Aerodynamics* 188, 151-160.

- Hunt, J., A. A. Wray and P. Moin (1988). Eddies, streams, and convergence zones in turbulent flows. *Studying Turbulence Using Numerical Simulation Databases*, 2.
- Jia, Y. X. and Y. G. Mei (2018). Numerical simulation of pressure waves induced by high-speed maglev trains passing through tunnels. *International Journal of Heat and Technology* 36(2), 687-696.
- Katsuya, YAMAMOTO, Yuichi, KOZUMA, Naoto, TAGAWA, Shiro, HOSAKA, Hiroki, TSUNODA (2004). Improving Maglev Vehicle Characteristics for the Yamanashi Test Line. *Quarterly Report of RTRI*.
- Lee, H. M., Z. M. Wang, K. M. Lim and H. P. Lee (2019). A Review of Active Noise Control Applications on Noise Barrier in Three-Dimensional/Open Space: Myths and Challenges. *Fluctuation And Noise Letters* 18(4), 1-21.
- Li, H., X. Z. Li and J. Zheng (2021). Vibration Characteristics of Fully Enclosed Sound Barriers on Railway Bridges under the Movement of Trains. *Advances in Civil Engineering* 2021, 1-14.
- Li, M. S., B. Lei, G. B. Lin, H. Q. Bi and F. M. Wang (2006). Field measurement of passing pressure and train induced airflow speed on high speed maglev vehicles. *Acta Aerodynamica Sinica* 24(2), 209-212. (In Chinese)
- Li, T., D. Qin, W. H. Zhang and J. Y. Zhang (2020). Study on the aerodynamic noise characteristics of high-speed pantographs with different strip spacings. *Journal of Wind Engineering and Industrial Aerodynamics* 202, 1-12.
- Li, X. B., G. Chen, Z. Wang, X. H. Xiong, X. F. Liang and J. Yin (2019). Dynamic analysis of the flow fields around single- and double-unit trains. *Journal of Wind Engineering and Industrial Aerodynamics* 188, 136-150.
- Lighthill, M. J. (1954). On Sound Generated Aerodynamically. II. Turbulence as a Source of Sound. *Proceedings of the Royal Society A: Mathematical, Physical and Engineering Sciences*.
- Lighthill, M. J. (1951). On Sound Generated Aerodynamically I. General Theory. *Proceedings of Royal Society of London Ser A* 211(1107), 564-587.
- Mellet, C., F. Letourneaux, F. Poisson and C. Talotte (2006). High speed train noise emission: Latest investigation of the aerodynamic/rolling noise contribution. *Journal of Sound and Vibration* 293(3-5), 535-546.
- Menter, F. R., M. Kuntz and R. Langtry (2003). Ten years of industrial experience with the SST turbulence model. *Heat and Mass Transfer* 4.
- Powell, A. (1964). Theory of Vortex Sound. *The Journal of the Acoustical Society of America* 36(1).
- Reddy, K. R., J. A. Ryon and P. A. Durbin (2014). A DDES model with a Smagorinsky-type eddy viscosity formulation and log-layer mismatch correction. *International Journal of Heat and Fluid Flow* 50, 103-113.
- Shur, M. L., P. R. Spalart, M. K. Strelets and A. K. Travin (2008). A hybrid RANS-LES approach with delayed-DES and wall-modelled LES capabilities. *International Journal of Heat and Fluid Flow* 29(6), 1638-1649.
- Spalart, P. R. (1997). Comments on the feasibility of LES for wings, and on a hybrid RANS/LES approach. *First AFOSR International Conference on DNS/LES*, Ruston, LA.
- Spalart, P. R., S. Deck, M. L. Shur, K. D. Squires, M. K. Strelets and A. Travin (2006). A new version of detached-eddy simulation, resistant to ambiguous grid densities. *Theoretical and Computational Fluid Dynamics* 20(3), 181-195.
- Su, J., Y. Sun and Y. Liu (2018). Complexity Study on the Unsteady Flow Field and Aerodynamic Noise of High-Speed Railways on Bridges. *Complexity*, 1-16.
- Sun, X. Q. and H. Xiao (2018). Numerical Modeling and Investigation on Aerodynamic Noise Characteristics of Pantographs in High-Speed Trains. *Complexity*, 1-12.
- Tan, X., T. Wang, B. Qian, B. Qin and Y. Lu (2019). Aerodynamic Noise Simulation and Quadrupole Noise Problem of 600km/h High-speed Train. *IEEE Access* (7), 124866-124875.
- Tan, X. M., H. F. Liu, Z. G. Yang, J. Zhang, Z. G. Wang and Y. W. Wu (2018). Characteristics and Mechanism Analysis of Aerodynamic Noise Sources for High-Speed Train in Tunnel. *Complexity*, 1-19.
- Thompson, D. J., E. L. Iglesias, X. Liu, J. Zhu and Z. Hu (2015). Recent developments in the prediction and control of aerodynamic noise from high-speed trains. *International Journal of Rail Transportation* 3(3), 119-150.
- Tyll, J. S., D. Liu, J. A. Schetz and J. F. Marchman (1996). Experimental studies of magnetic levitation train aerodynamics. *AIAA Journal* 34(12), 2465-2470.
- Wen, W. Q., K. N. Lei, D. W. Yang and X. Z. Li (2021). A Full-scale Model Test of Noise Reduction Performance of Fully-enclosed Noise Barriers on High-speed Railway. *Journal of the China Railway Society* 43(3), 193-199. (In Chinese)
- Xia, C., H. F. Wang, X. Z. Shan, Z. G. Yang and Q. L. Li (2017). Effects of ground configurations on the slipstream and near wake of a high-speed train. *Journal of Wind Engineering and Industrial Aerodynamics* 168, 177-189.
- Zhang, J., Y. Wu, J. Gao, G. Gao and Z. Yang (2021). Numerical Simulation of Aerodynamic Noise Characteristics of High-Speed Maglev Train with a Speed of 600 km/h. *China Railway*

Science 42(6), 112-121. (In Chinese).

- Zhang, X., R. Liu, Z. Y. Cao, X. Y. Wang and X. Z. Li (2019). Acoustic performance of a semi-closed noise barrier installed on a high-speed railway bridge: Measurement and analysis considering actual service conditions. *Measurement* 138, 386-399.
- Zheng, J., X. Z. Li, X. B. Zhang, R. Bi and X. W. Qiu (2022). Structure-borne noise of fully enclosed sound barriers composed of engineered cementitious composites on high-speed railway bridges. *Applied Acoustics* 192, 1-15.
- Zheng, J., D. Liu, X. Li, R. Bi, Z. Gong and Z. Hu (2021). Experimental and Numerical Research on Noise Reduction Performance of Fully Enclosed Sound Barriers on High-speed Railway Bridges. *China Journal of Highway and Transport* 34(4), 152-161. (In Chinese)
- Zhou, P., T. Li, C. F. Zhao and J. Y. Zhang (2020). Numerical study on the flow field characteristics of the new high-speed maglev train in open air. *Journal of Zhejiang University-SCIENCE A* 21(5), 366-381.